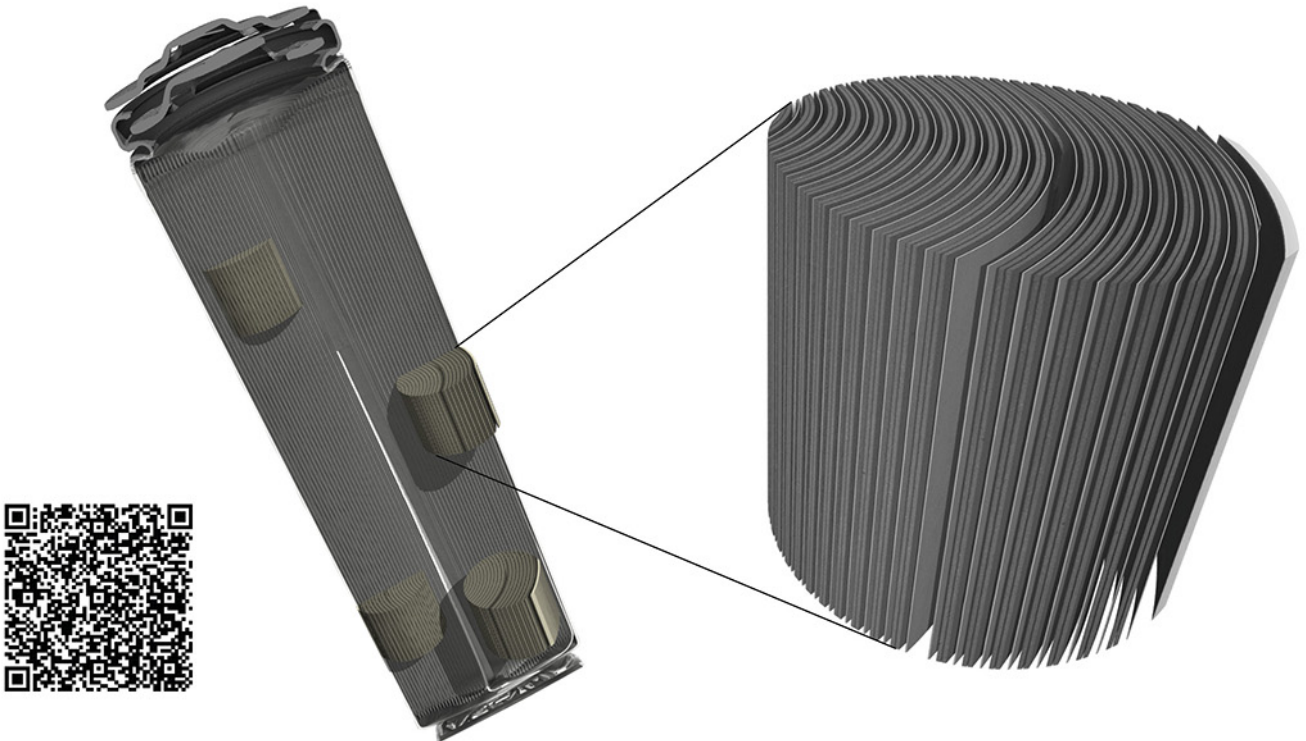# TESCAN micro-CT solutions for energy storage materials research

TESCAN UniTOM XL

✓ Multi-scale non-destructive 3D imaging optimized to maximize throughput and contrast

✓ Fast scanning and high sample throughput with temporal resolutions below 10 seconds

✓ Wide array of samples types

✓ Enables dynamic tomography and *in-situ* experiments

✓ Dynamic screening for synchrotron beamtime

✓ Modular and open system with unmatched flexibility for research

Click and find out more

Enhancing Output Performance of Triboelectric Nanogenerator via Charge Clamping

Jianlong Wang, Xin Yu, Da Zhao, Yang Yu, Qi Gao, Tinghai Cheng,* and Zhong Lin Wang*

As a microenergy harvesting device, the output performance of triboelectric nanogenerators (TENGs) has long been limited by their surface charges. In this work, an enhancement of the output performance of TENGs via charge clamping (CC-TENG) is proposed. The device is comprised of a mechanical-switch direct-current TENG (MDC-TENG), charge clamping module (CCM), and main-TENG. During operation, the CCM is employed to accumulate and clamp the unidirectional charge generated by the MDC-TENG. And then, the accumulated charges flow between CCM and main-TENG. With the increase of transferred charges, the output performance can be effectively improved. In addition, the MDC-TENG is employed to reduce both power dissipation and circuit complexity. Furthermore, an integrated device based on the CC-TENG is demonstrated which harvests wind energy and attains a charge output of 1.01 µC. Moreover, a multimode coupling is adopted, that is, an alternating-current TENG operating in contact-separation mode and a direct-current TENG operating in a lateral-sliding mode that can be employed in environments for which multiple motions coexist. The device provides a reference to improve output performance in the context of wind energy capture.

1. Introduction

With the rapid development of sensor technologies and implantable devices, there is a great demand for energy harvesting devices that output milliwatt/microwatt electric power. In recent years, various energy harvesting technologies have emerged one after another.[1] At present, the energy industry is developing smaller and more suitable energy harvesting technologies.[2] Among them, many technologies utilize mechanical motion to generate electric energy, including piezoelectric power generators,[3] electromagnetic power generators,[4] and photovoltaic power generators.[5]

Invented by Wang's group in 2012, triboelectric nanogenerators (TENGs), which are based on the coupling of the triboelectric effect and electrostatic induction,[6] have attracted much attention because of the extensive range in the selection of materials, small size, and great potential in converting mechanical energy into electric energy.[7] However, for conventional TENGs based on the contact-separation mode, the inductive charges that affect the output of TENG are confined to the surface of the dielectric layer. To date, methods to enhance the output performance mainly focus on ionized-air injection,[8] surface structure control and chemical modification,[9] power management module,[10] structure optimization,[11] and the selection of materials.[12] The charges arising from these methods are static and therefore neither realize the maximum charge output nor achieve long-term operation. Therefore, a charge-pumping TENG is proposed that adopts a floating layer to accumulate and bind charges,[13] or use an external capacitor to excite charges directly on the electrodes,[14] thereby achieving a high and stable output performance. However, the pump-TENG in the charge-pumping TENG produces a direct-current (DC) output through rectifier diodes that is a dissipative element that not only dissipates power but also increases circuit complexity.[15] And it is significant to develop a strategy to enhance the output performance, decrease the power dissipation and circuit complexity, and design the integrated device to achieve the practical application of this strategy in the wind environment.

Hence, an enhancing output performance of TENG via charge clamping (CC-TENG) is proposed in this paper, which is comprised of mechanical-switch DC TENG (MDC-TENG), charge clamping module (CCM), and main-TENG. In particular, CCM can be divided into three parts: an external capacitor to accumulate the charges generated by the MDC-TENG, Zener diodes for clamping the accumulated charges, and protective resistors. The accumulated charges flow in the loop circuit formed by the main-TENG and CCM, achieving an enhancement in the output performance. In addition, the adoption of the MDC-TENG reduces to some extent both the complexity of the circuit and the power dissipation caused

J. Wang, Dr. X. Yu, D. Zhao, Y. Yu, Q. Gao, Prof. T. Cheng, Prof. Z. L. Wang
Beijing Institute of Nanoenergy and Nanosystems
Chinese Academy of Sciences
Beijing 101400, China
E-mail: chengtinghai@binn.cas.cn; zhong.wang@mse.gatech.edu
J. Wang, D. Zhao, Y. Yu, Prof. T. Cheng
School of Mechatronic Engineering
Changchun University of Technology
Changchun, Jilin 130012, China
Prof. T. Cheng, Prof. Z. L. Wang
CUSTech Institute
Wenzhou, Zhejiang 325024, China
Prof. Z. L. Wang
School of Materials Science and Engineering
Georgia Institute of Technology
Atlanta, GA 30332-0245, USA

**ADVANCED
SCIENCE NEWS**
www.advancedsciencenews.com

**ADVANCED
ENERGY
MATERIALS**
www.advenergymat.de

by the rectifier diodes. Moreover, the proposed MDC-TENG solves the problem of charge backflow during charge injection. To demonstrate the capability of CC-TENG in practical applications, an integrated device based on the CC-TENG is fabricated and measured for wind energy harvesting. The experimental results indicate that the integrated device can produce ≈1300 V, 110 μA, 1.01 μC, and 25.96 mW, which can stably supply power to a hygrothermograph in the simulated wind environment. Moreover, the multimode coupling is employed in the integrated device, that is, the combination of alternating-current TENG applied as the main-TENG and MDC-TENG, as well as the coexistence of contact-separation mode and lateral-sliding mode. All in all, the device represents a reliable approach to enhancing the output performance of TENGs in practical applications.

2. Results and Discussion

2.1. Composition and Working Mechanism of Charge Clamping TENG

The CC-TENG (**Figure 1**a(i)) is mainly comprised of charge source, CCM, and main-TENG. The CCM contains the following three parts: an external capacitor to accumulate charges, several Zener diodes to clamp charges, and protective resistors. First, the unidirectional charge generated by the direct-current TENG (DC-TENG) is accumulated to the CCM. And then, the conventional TENG based on the contact-separation mode is used as the main-TENG, and the accumulated charges directly act on the electrode of the main-TENG. The main-TENG has equivalent capacitance inside, whose gap distance affects the capacitance of its internal capacitor. Therefore, the change of

gap distance makes the accumulated charge flow between CCM and main-TENG, the purpose being to achieve an enhancement in the output performance (see Figure 1a(ii)).

The working principle of the CC-TENG (Figure 1b) has two working stages. In the initial stage, the unidirectional charges generated by the DC-TENG are injected into the CCM. Because the TENGs have the characteristics of large voltage and small current, unlike the electromagnetic generator, it takes several working cycles for the external capacitor to be fully charged. In particular, with increasing gap distance between the two plates, the equivalent capacitance of the main-TENG decreases. Therefore, the accumulated charges in the CCM are pumped into the main-TENG in the contact process, and the charges in the main-TENG flow back to the CCM in the separation process for the main-TENG. In the second stage, the unidirectional charges generated by the DC-TENG are continuously injected into the CCM. Finally, the CC-TENG reaches a stable condition, thereby achieving the objection, that being enhancing the output performance.

2.2. Working Mechanism and Device Structure

To design a suitable DC-TENG, a simulation model based on pipelines is developed to analyze and guide this work (Figure S1, Supporting Information). In terms of CC-TENG, charge backflow appears because the charge source and the external capacitor appear with equal potentials. Therefore, when the DC-TENG is replaced as a charge source by the DC high voltage power supply, charges cannot be injected into the main-TENG when the potentials at both ends of the charge source and the external capacitor reach equilibrium. Taking a water pipeline as an example, when the inflow and outflow
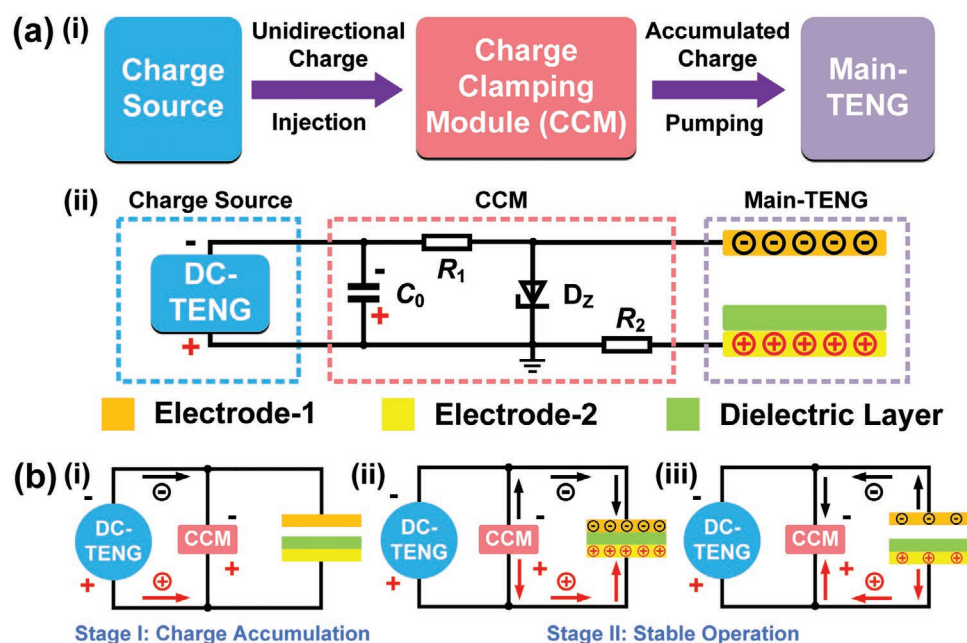

Figure 1. Composition and working principle of the CC-TENG. a,i) The composition and ii) circuit diagram of the CC-TENG. b) The working mechanism of the CC-TENG.
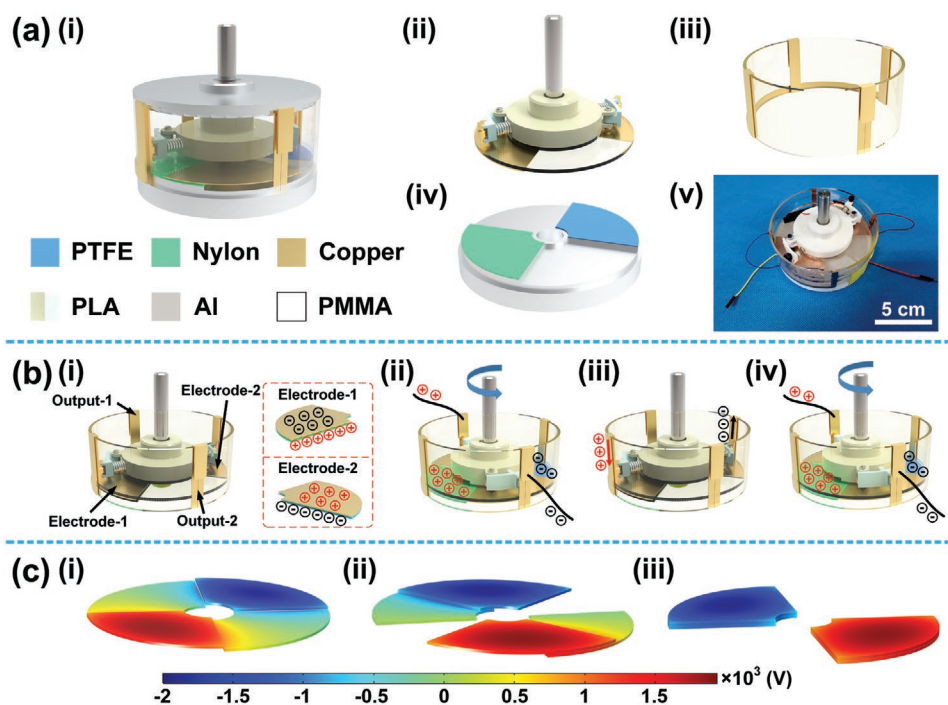
**ADVANCED
SCIENCE NEWS**

www.advancedsciencenews.com

**ADVANCED
ENERGY
MATERIALS**

www.advenergymat.de

Figure 2. Structure, working mechanism, and simulated potential distribution. a) The structure photography of MDC-TENG. b) The working mechanism of MDC-TENG. c) The simulated potential distribution of MDC-TENG.

in two pools are almost identical, that is, the charges injected into the external capacitor are almost equal in number with the released charge, the charge accumulation strategy does not work. As a result, the output performance of the main-TENG cannot be fully improved. Enhancements in the main-TENG performance are only affected by the charge source. Therefore, a rectifier diode is adopted, its function being to provide unidirectional conduction and suppression of the charge backflow, similar to the unidirectional device in a water pipeline.

Therefore, a MDC-TENG is reported in this paper, which is comprised of a rotor, a stator, and electric conducting components (**Figure 2**a(i)). Electrodes and a rolling brush constitute the rotor and are connected using a wire (Figure 2a(ii)). For the electric conducting components, two output terminals and a transmission bridge are fixed to the acrylic tube (Figure 2a(iii)). The stator used is composed of a substrate of nylon film and polytetrafluoroethylene (PTFE) film (Figure 2a(iv)). It assists the MDC-TENG in producing a DC output as well as protecting the internal mechanical structures and power generation units. Figure 2a(v) shows images of the as-fabricated MDC-TENG; its working principle is illustrated in Figure 2b. In the initial stage, electrode-1 and electrode-2 make contact with the nylon film and the PTFE film, respectively. In accordance with the triboelectric sequence table, the electrodes of the nylon film and the PTFE film are charged positively and negatively. With the rotation of the rotor, the accumulated charges are discharged through two output terminals, and a DC output is generated in the second stage. In the next stage, electrode-1 and electrode-2 of opposite polarity mutually slide over the dielectric layer. When they are in full contact again, the negative

charges induced by the nylon film flows to the end of PTFE film through the transmission bridge because of a difference in potential at both ends. In the process, electrostatic charges are accumulated, establishing a high output voltage. In the final stage, these charges are released again, and a unidirectional output is generated, thereby completing one working cycle. In addition, the simulated potential distribution of MDC-TENG is depicted in Figure 2c. The simulated potential distribution of MDC-TENG is depicted in Figure 2c. The model adopted in COMSOL Multiphysics software is composed of PTFE, Nylon, and Cu textile (electrode), whose potential distribution is simulated, maintaining their inherent properties. And simulation conditions of model are identical with the experimental environment that is the temperature of 298.15 K and the atmospheric pressure of 1 atm.

The MDC-TENG realizes DC output without rectifier diodes and overcomes the problem of charge backflow. Similar to the switch device in Figure S1c in the Supporting Information, the MDC-TENG accumulates charges and releases them. Using a mechanical-switch, the working process of the MDC-TENG involves two stages: charge accumulation and charge release. During charge accumulation, the potential difference between the two ends of the MDC-TENG increases continuously. At the moment of charge release, the potential across the MDC-TENG is higher than that across the external capacitor. Hence, the excitation charges generated by the MDC-TENG are injected into the CCM. Next, the MDC-TENG enters the charge accumulation stage again and the mechanical switch is turned off. At the moment, charge backflow is cut off so that all charges from the CCM can be injected into the main-TENG.

ADVANCED
SCIENCE NEWS
www.advancedsciencenews.com

ADVANCED
ENERGY
MATERIALS
www.advenergymat.de

2.3. The Output Performance Measurement of MDC-TENG and Main-TENG

Using the MDC-TENG as the charge source, the output performance is obtained (**Figure 3**a). Because the electrometer (Model 6514 System, Keithley) is a capacitive device, the voltage and charge in a sole direction are in an accumulative state. In particular, the working mechanism of the MDC-TENG involves charges being accumulated and then released. Hence, the charging curve remains stable when charges accumulate and rises when charges are released. As a result, intermittent rises in the curve occur at different excitation frequencies. The same is true for the voltage curve. Because of the potential difference, the voltage curve shows a reverse state. Moreover, the rotating speed has no impact on the amplitude of the released charges and thereby, the current remains at ≈10 μA all the time (see Figure 3a(ii)).

The working principle and simulated potential distribution of the single main-TENG without the assistance of the MDC-TENG and the CCM are shown in Figure S2 in the Supporting Information. And the output performance of the main-TENG is presented under different operating frequencies. The experimental results show that limited by surface static charges, the main-TENG can produce about 10 V, 0.9 μA, and 10 nC under the excitation of frequency 3 Hz (see Figure 3b).

2.4. The Optimized Parameters and Output Performance of CC-TENG

To understand better the fundamental characteristics of the CC-TENG, some influence factors are investigated, including the selection of electronic components, structural parameters, and the output performance. In addition, a theoretical model involving a loop circuit composed of an external capacitor

and an equivalent capacitance model of main-TENG is established to analyze the output performance of the main-TENG (Figure S3, Supporting Information). To demonstrate the output performance quantitatively, the charge $Q(x)$ and the voltage of the air gap V_{gap} can be expressed as

$$Q(x) = Q \cdot \frac{d + \frac{\varepsilon_0 \varepsilon_r S}{C_0}}{d + x(t)\varepsilon_r} \tag{1}$$

$$V_{gap} = \frac{x(t)\sigma}{\varepsilon_0} \cdot \frac{d + \frac{\varepsilon_0 \varepsilon_r S}{C_0}}{d + x(t)\varepsilon_r} \tag{2}$$

where ε_r and ε_0 denote the relative permittivity and vacuum permittivity of the material, respectively, Q and σ the charge and charge density of the main-TENG in the contact state, respectively. S denotes the effective contact area, $x(t)$ is the gap distance of two plates, and d is the thickness of the dielectric layer.

As shown in **Figure 4**, the circuit and structural parameters of CC-TENG are systematically investigated and the output performance measurement is also conducted. A charge clamping system is constructed to explore the optimal matching capacitor. For the sake of simplicity, a high voltage DC power supply is used as the charge source to replace the MDC-TENG. The working principle of the CC-TENG based on the voltage resources is illustrated in Figure S4 in the Supporting Information. Furthermore, to prevent instantaneous currents exceeding 20 mA through dielectric breakdown from damaging the measurement instrument, a current limiting resistor R_1 with resistance of 200 kΩ and one resistor R_2 with resistance of 5 GΩ are inserted into the circuit in series and parallel, respectively. With an excitation frequency applied to the main-TENG set to 1 Hz, various bias voltages are applied to the main-TENG, and
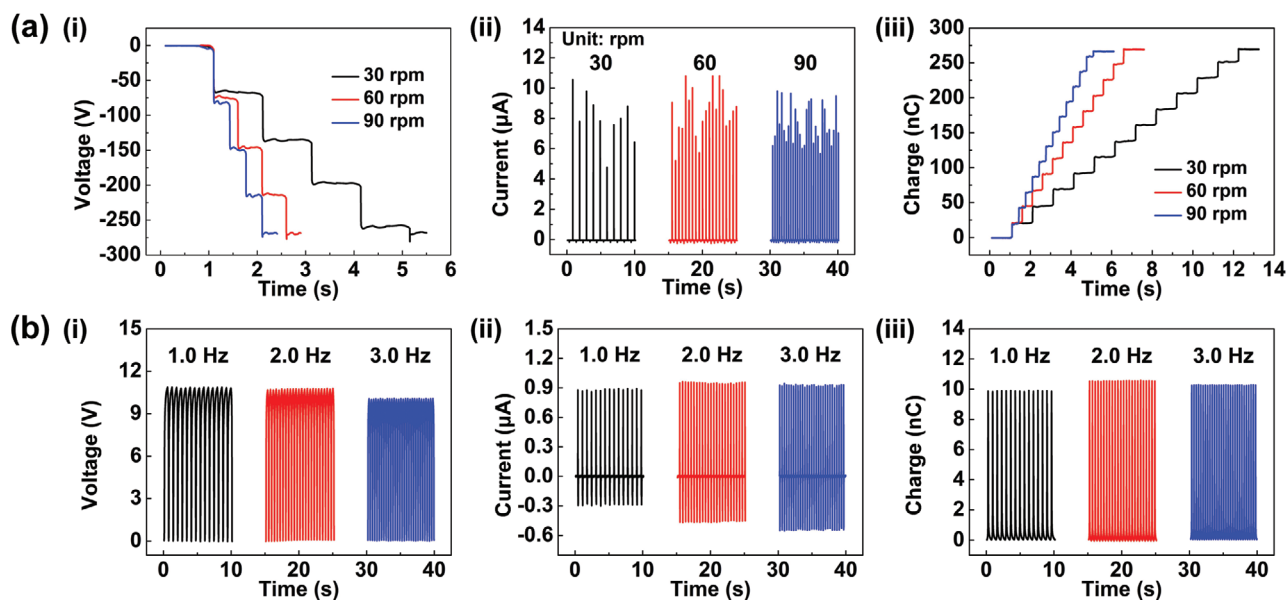

Figure 3. The output performance measurement of MDC-TENG and main-TENG. a) Output performance of MDC-TENG under different operating frequencies. b) Output performance of main-TENG under different operating frequencies.
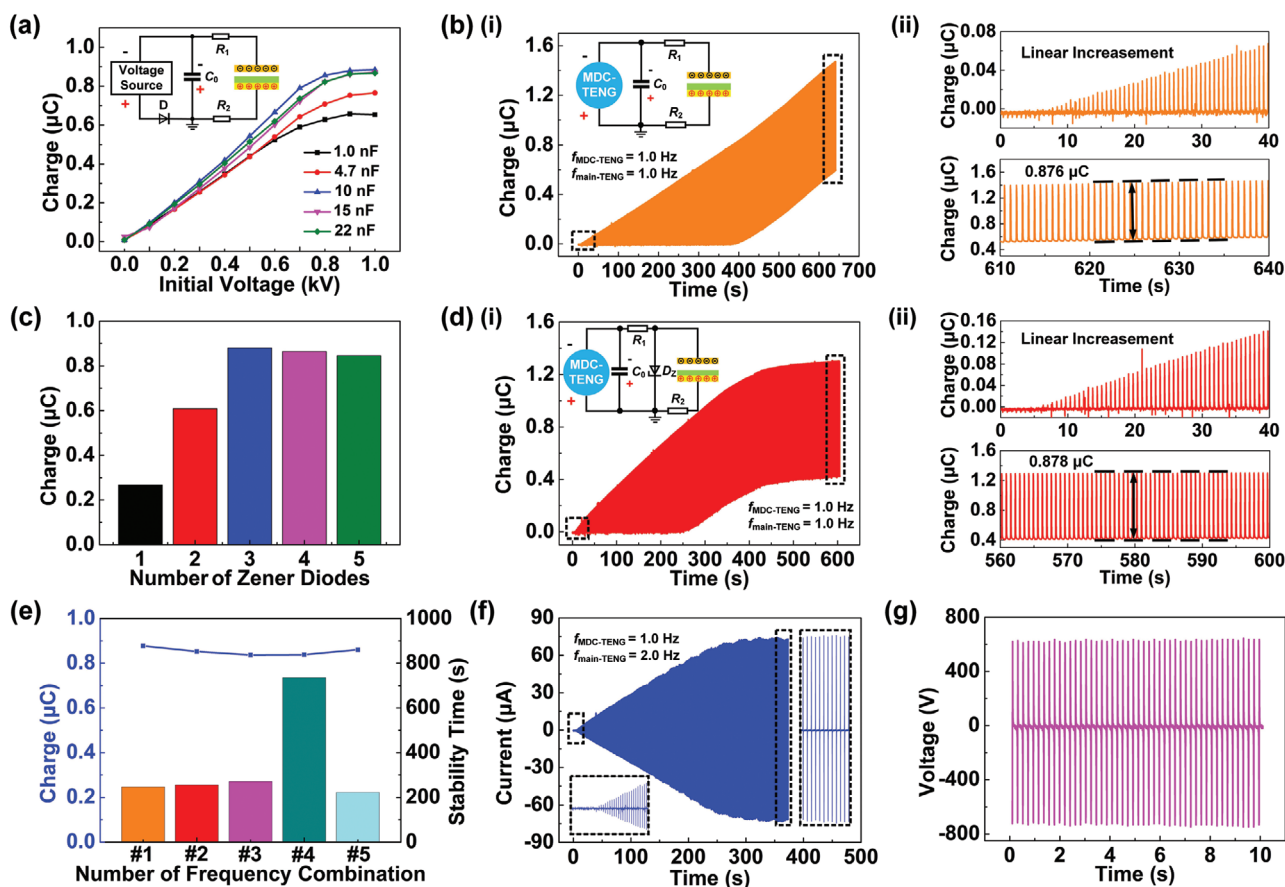
Figure 4. Electric output measurement of the CC-TENG. a) Charge curves of the main-TENG with different capacitors applied with various initial voltages using a high-voltage source. b,i) Output charges of the CC-TENG without using rectifier diodes and ii) enlarged initial charge accumulation curve (top) and saturation output condition (bottom). c) Output charges comparison of the CC-TENG with different numbers of Zener diodes. d,i) Output charges from the CC-TENG with three Zener diodes and ii) enlarged initial charge accumulation curve (top) and saturation output condition (bottom). e) Output charges comparison when the combination of different frequencies adopted by the CC-TENG. f,g) Output current and voltage of the CC-TENG.

charge curves for various capacitors are obtained (Figure 4a). The experimental results show that a maximum charge is reached when the capacitance exceeded 10 nF; the output performance remains almost unchanged when the bias voltage exceeded 800 V. The number of excitation charges, which is determined by the external capacitor acting on both ends of the main-TENG, directly affects the output (Note S1, Supporting Information). In addition, the other output performance measurement results are shown in the Figure S5 in the Supporting Information.

And then, an MDC-TENG is employed to analyze the influence of the number of Zener diodes on the output, and the excitation frequencies of the main-TENG and MDC-TENG are set to 1 Hz, respectively (Figure 4b–d). From the enlarged initial and saturated states (Figure 4b), the charge output is unstable and dielectric air breakdown appeared accordingly. To avoid possible air breakdown and to stabilize the voltage, different numbers of Zener diodes are applied in the external circuit (Figure S6, Supporting Information). To overcome the influence incurred when a reverse current that is too large or too small occurs in the Zener diode, a resistor must be connected in series in the regulator circuit to limit the current and ensure

normal operations for the Zener diode. The matching relationship between the current limiting resistor R_1 and the number of Zener diodes and the theoretical analysis of the voltage stabilizing circuit (Table S1 and Note S2, Supporting Information) show that a single Zener diode limits the output of CC-TENG significantly, but with an increasing number of Zener diodes in series, the output performance gradually diminishes. Indeed, with their total number increasing, the output performance decreases slightly because Zener diodes are energy-consuming components (Figure 4c). In particular, the charge accumulation of the CC-TENG with three Zener diodes used in the external circuit is shown in Figure 4d(i). From the enlarged initial and saturated states (Figure 4d(ii)), a stabilizing voltage is achieved, and the energy dissipation from the Zener diodes is almost negligible.

With an idea of multimode coupling adopted in the CC-TENG, the main-TENG generating the alternating current output operates in the contact-separation mode while the MDC-TENG producing the DC output operates in the lateral-sliding mode. For the CC-TENG, we need then to investigate the frequency matching relationship between the main-TENG and MDC-TENG. Figure 4e exhibits the

**ADVANCED
SCIENCE NEWS**

www.advancedsciencenews.com

**ADVANCED
ENERGY
MATERIALS**

www.advenergymat.de

charge output of the CC-TENG and time required to reach saturation when the MDC-TENG and the main-TENG adopt different frequency combinations respectively. The combination of different frequencies adopted by the MDC-TENG and the main-TENG respectively are shown in Table S2 in the Supporting Information. First, the frequency of the MDC-TENG is simultaneously set to 1 Hz, while the frequency of the main-TENG is varied. As the frequency of the main-TENG changes, the output performance of the CC-TENG and the time required to reach a saturation output condition remains almost unchanged. Next, the frequency of the main-TENG is set to 1 Hz and the frequency of the MDC-TENG is varied. In particular, as the frequency of the MDC-TENG increases, the time required to reach the saturation output condition of CC-TENG is shortened. In contrast, as the frequency of the MDC-TENG decreases, the time to reach the saturation output condition is extended. In summary, when the external circuit and environmental condition remain unchanged, the output performance of the CC-TENG is not affected by any factors, and the excitation frequency applied to the MDC-TENG affects the time required to reach saturation output directly. Although a high frequency ratio will increase current output, it will cause instability of the mechanical structure. Therefore, the frequency ratio between MDC-TENG and main-TENG is set to 1:2 for the subsequent design of the integrated device. And when the frequencies of the MDC-TENG and the main-TENG are set to 1 and 2 Hz, respectively, the current and voltage of the CC-TENG reached 74 µA and 1200 V (Figure 4f,g).

2.5. Structure, Performance, and Application of the Integrated Device

To enhance the charge clamping strategy in practical applications, the integrated device based on the CC-TENG is fabricated to harvest wind energy. This device is mainly composed of MDC-TENG, CCM, and main-TENG (**Figure 5**a(i)). A photograph of the fabricated integrated device is demonstrated in Figure 5b. In addition, the flange turntable with cam structure and the MDC-TENG share the same shaft; a follower embedded with an electrode plate is attached to the frame by four screws (Figure 5a(ii)). When operating the MDC-TENG, the flange turntable fixed to the shaft drives the follower forward using the cam structure. The stroke of the cam structure is the same as the gap distance between the two electrode plates. When the main-TENG is in the state of full contact, the two electrode plates separate again because of the resilience of the spring, thereby completing the working cycle. In addition, there exists two cam structures on the follower, thereby realizing the enhancement in machinery frequency. Photographs of the main-TENG parts in the integrated device are given in Figure S7 in the Supporting Information.

When the external excitation frequency is set to 1.5 Hz, the working frequency of the MDC-TENG and the main-TENG are 1.5 and 3 Hz, respectively, because of the enhancement in machinery frequency. At the moment, the integrated device produces ≈1300 V, 110 µA, and 1.01 µC in atmospheric environments (Figure 5c–e). In particular, due to the mechanical assembly error, the force when the two plates are in contact
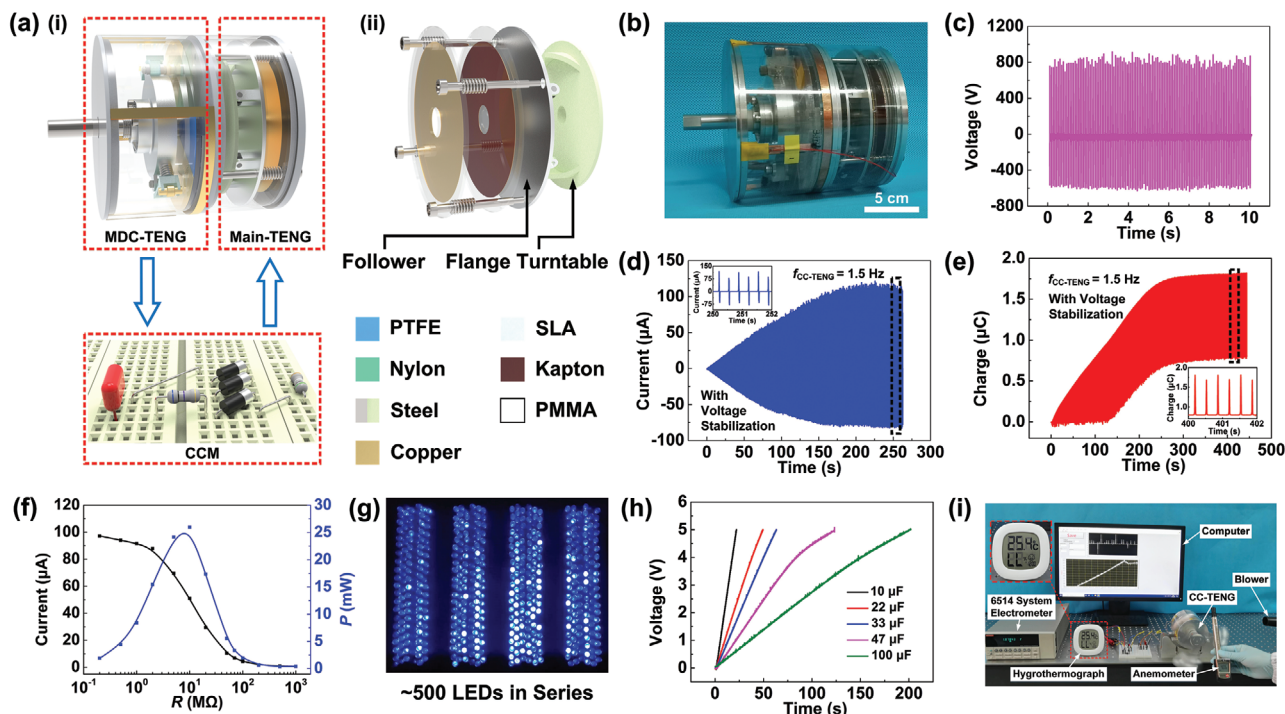

Figure 5. Structure, performance, and application of the integrated device. a,i) Schematic of the integrated device based on the CC-TENG and ii) the enlarged diagram of the main-TENG. b) Photograph of the fabricated integrated device. Scale bar, 5 cm. c–e) Output performance measurement of the integrated device. f) Output current and peak power under various external loads. g) Illumination of ≈500 LEDs. h) Charging curve of the capacitor using the integrated device. i) The integrated device powering a commercial hygrothermograph.

**ADVANCED
SCIENCE NEWS**
www.advancedsciencenews.com

**ADVANCED
ENERGY
MATERIALS**
www.advenergymat.de

increases and thereby, the output charge is higher than that when the linear motor is used as the excitation source of the main TENG. Moreover, the peak power of the CC-TENG is measured with various external load resistances. Because the working frequency of the main-TENG increases, the output current increases accordingly and thereby, the peak power can reach up to 25.96 mW when the matching resistance is 10 MΩ (Figure 5f). In addition, ≈500 light-emitting diodes (LEDs) are illuminated by the CC-TENG (Figure 5g and Video S1, Supporting Information). Figure 5h presents the time-dependence of the voltage for the integrated device when charging capacitors of different capacitances; the specific circuit diagram is presented in Figure S8 in the Supporting Information. In addition, to demonstrate the output performance of the CC-TENG in practical applications, a commercial hygrothermograph is powered under the simulated wind environment of about 5 m s^{-1} (Figure 5i and Video S2, Supporting Information).

3. Conclusions

The CC-TENG is proposed, which is comprised of MDC-TENG, CCM, and main-TENG. The CCM is used to accumulate and clamp the charges generated by the MDC-TENG and then pump the charge into the main-TENG. Due to the increase of transferred charge between CCM and main-TENG, the output performance of CC-TENG is effectively improved. In particular, MDC-TENG can produce a direct-current output without the need for rectifier diodes, thereby reducing the power dissipation and circuit complexity. Moreover, the charge backflow problem during charge injection is solved by incorporating mechanical-switch. For practical applications, an integrated device based on the CC-TENG is proposed for wind energy harvesting. The as-fabricated device produces a charge output of 1.01 μC and a peak power output of 25.96 mW under the excitation of frequency 1.5 Hz. And a commercial hygrothermograph is steadily powered in the stimulated wind environment. In addition, the idea of multimode coupling is adopted to apply CC-TENG in complex environments with different states of motion. In summary, the CC-TENG significantly improved the output performance of the wind harvester in environments where multiple dynamics coexist.

4. Experimental Section

Fabrication of the Main-TENG: Two pieces of annular acrylic plates with dimensions of 90 mm (external diameter) × 20 mm (inner diameter) × 1 mm (thickness) are processed as the substrates of main-TENG by a carbon dioxide laser cutting machine (31 Degree 6090). For one piece of acrylic plate, a foam with dimensions of 80 mm (external diameter) × 20 mm (inner diameter) × 1 mm (thickness), which is adhered to the acrylic plates, is coated with the copper electrode. For another acrylic plate, a 50 μm thick Kapton film covers another copper electrode which is assembled in the acrylic plate. The produced effective contact area between them is 80 mm (external diameter) × 20 mm (inner diameter).

Fabrication of the MDC-TENG: An 80 μm thick PTFE film and a 25 μm thick nylon film with the identical area (a quarter of 95 mm (external diameter) × 20 mm (inner diameter)) adhere to the as-prepared acrylic substrate in a diagonal form. Copper electrodes with the same area size and arrangement adhere to another acrylic plate. Acrylic tubes

with dimensions of 100 mm (external diameter) × 96 mm (inner diameter) × 50 mm (length) are used as the shell of MDC-TENG, respectively. In terms of mechanical structure, the support, end cover, roller, etc., are machined by a milling machine. For the external circuit, a commercial capacitor (CBB81) and several Zener diodes (3EZ400D5) are connected with the MDC-TENG in parallel to avoid air breakdown. In addition, the high-voltage direct-current power and the main-TENG are connected through a rectifier diode (1N4007).

Characterization and Measurements: A two-phase hybrid stepping motor (HOHI 57BYGH56D8EIS-P) is adopted as the rotary power source. The excitation in linear direction is generated by a linear motor (LinMot B01-37 × 166/160). The output performance of the main-TENG and MDC-TENG, as well as the short-circuit current and transferred charge of CC-TENG, are measured by a system electrometer (Keithley 6514). A mixed domain oscilloscope (Tektronix MDO4054B-3) with a passive high voltage probe (Tektronix P6015A) is used to measure the open-circuit voltage of CC-TENG. A high-voltage direct-current power (Keithley 6517) is employed to provide the voltage source for the main-TENG. An electric blower (Dongcheng Q1F-FF-32) is applied to generate the simulated wind environment.

Supporting Information

Supporting Information is available from the Wiley Online Library or from the author.

Conflict of Interest

The authors declare no conflict of interest.

Data Availability Statement

The data that support the plots within this paper and other findings of this study are available from the corresponding authors upon reasonable request.

[1] J. Chen, Z. L. Wang, *Joule* **2017**, *1*, 480.
[2] L. Xu, L. Xu, J. Luo, Y. Yan, B.-E. Jia, X. Yang, Y. Gao, Z. L. Wang, *Adv. Energy Mater.* **2020**, *10*, 2001669.
[3] Z. Yang, S. Zhou, J. Zu, D. Inman, *Joule* **2018**, *2*, 642.
[4] H. Song, D. R. Patil, W.-H. Yoon, K.-H. Kim, C. Choi, J.-H. Kim, G.-T. Hwang, D.-Y. Jeong, J. Ryu, *Energy Environ. Sci.* **2020**, *13*, 4238.

ADVANCED
SCIENCE NEWS

www.advancedsciencenews.com

ADVANCED
ENERGY
MATERIALS

www.advenergymat.de

[5] S. A. Hashemi, S. Ramakrishna, A. G. Aberle, *Energy Environ. Sci.* **2020**, *13*, 685.

[6] a) F.-R. Fan, Z.-Q. Tian, Z. Lin Wang, *Nano Energy* **2012**, *1*, 328; b) Z. L. Wang, *Faraday Discuss.* **2014**, *176*, 447; c) Z. L. Wang, *Mater. Today* **2017**, *20*, 74; d) Z. L. Wang, *Nano Energy* **2018**, *54*, 477; e) Z. L. Wang, A. C. Wang, *Mater. Today* **2019**, *30*, 34; f) Z. L. Wang, *Nano Energy* **2020**, *68*, 104272.

[7] a) C. Wu, A. C. Wang, W. Ding, H. Guo, Z. L. Wang, *Adv. Energy Mater.* **2019**, *9*, 1802906; b) Z. L. Wang, *Adv. Energy Mater.* **2020**, *10*, 2000137; c) R. Hinchet, H.-J. Yoon, H. Ryu, M.-K. Kim, E.-K. Choi, D.-S. Kim, S.-W. Kim, *Science* **2019**, *365*, 491; d) W. Xu, H. Zheng, Y. Liu, X. Zhou, C. Zhang, Y. Song, X. Deng, M. Leung, Z. Yang, R. X. Xu, Z. L. Wang, X. C. Zeng, Z. Wang, *Nature* **2020**, *578*, 392; e) H. Wang, J. Zhu, T. He, Z. Zhang, C. Lee, *Nano Energy* **2020**, *78*, 105241; f) P. Chen, J. An, S. Shu, R. Cheng, J. Nie, T. Jiang, Z. L. Wang, *Adv. Energy Mater.* **2021**, *11*, 2003066; g) J. Yu, G. Gao, J. Huang, X. Yang, J. Han, H. Zhang, Y. Chen, C. Zhao, Q. Sun, Z. L. Wang, *Nat. Commun.* **2021**, *12*, 1581.

[8] a) S. Wang, Y. Xie, S. Niu, L. Lin, C. Liu, Y. S. Zhou, Z. L. Wang, *Adv. Mater.* **2014**, *26*, 6720; b) H. Guo, J. Chen, M.-H. Yeh, X. Fan, Z. Wen, Z. Li, C. Hu, Z. L. Wang, *ACS Nano* **2015**, *9*, 5577.

[9] J. Chun, B. U. Ye, J. W. Lee, D. Choi, C.-Y. Kang, S.-W. Kim, Z. L. Wang, J. M. Baik, *Nat. Commun.* **2016**, *7*, 12985.

[10] Z. Wang, W. Liu, W. He, H. Guo, L. Long, Y. Xi, X. Wang, A. Liu, C. Hu, *Joule* **2021**, *5*, 441.

[11] R. Lei, Y. Shi, Y. Ding, J. Nie, S. Li, F. Wang, H. Zhai, X. Chen, Z. L. Wang, *Energy Environ. Sci.* **2020**, *13*, 2178.

[12] H. Zou, Y. Zhang, L. Guo, P. Wang, X. He, G. Dai, H. Zheng, C. Chen, A. C. Wang, C. Xu, Z. L. Wang, *Nat. Commun.* **2019**, *10*, 1427.

[13] a) L. Cheng, Q. Xu, Y. Zheng, X. Jia, Y. Qin, *Nat. Commun.* **2018**, *9*, 3773; b) L. Xu, T. Z. Bu, X. D. Yang, C. Zhang, Z. L. Wang, *Nano Energy* **2018**, *49*, 625; c) Y. Bai, L. Xu, S. Lin, J. Luo, H. Qin, K. Han, Z. L. Wang, *Adv. Energy Mater.* **2020**, *10*, 2000605.

[14] a) X. Liang, T. Jiang, Y. Feng, P. Lu, J. An, Z. L. Wang, *Adv. Energy Mater.* **2020**, *10*, 2002123; b) Y. Li, Z. Zhao, L. Liu, L. Zhou, D. Liu, S. Li, S. Chen, Y. Dai, J. Wang, Z. L. Wang, *Adv. Energy Mater.* **2021**, n/a, 2100050; c) W. Liu, Z. Wang, G. Wang, G. Liu, J. Chen, X. Pu, Y. Xi, X. Wang, H. Guo, C. Hu, Z. L. Wang, *Nat. Commun.* **2019**, *10*, 1426; d) H. Wang, L. Xu, Y. Bai, Z. L. Wang, *Nat. Commun.* **2020**, *11*, 4203; e) Y. Liu, W. Liu, Z. Wang, W. He, Q. Tang, Y. Xi, X. Wang, H. Guo, C. Hu, *Nat. Commun.* **2020**, *11*, 1599; f) W. Liu, Z. Wang, C. Hu, *Mater. Today* **2021**, *45*, 93.

[15] a) H. Ryu, J. H. Lee, U. Khan, S. S. Kwak, R. Hinchet, S.-W. Kim, *Energy Environ. Sci.* **2018**, *11*, 2057; b) J. Wang, Z. Wu, L. Pan, R. Gao, B. Zhang, L. Yang, H. Guo, R. Liao, Z. L. Wang, *ACS Nano* **2019**, *13*, 2587; c) Y. Song, N. Wang, Y. Wang, R. Zhang, H. Olin, Y. Yang, *Adv. Energy Mater.* **2020**, *10*, 2002756; d) H.-J. Yoon, M. Kang, W. Seung, S. S. Kwak, J. Kim, H. T. Kim, S.-W. Kim, *Adv. Energy Mater.* **2020**, *10*, 2000730; e) J. Wang, Y. Li, Z. Xie, Y. Xu, J. Zhou, T. Cheng, H. Zhao, Z. L. Wang, *Adv. Energy Mater.* **2020**, *10*, 1904227; f) J. Zhu, H. Wang, Z. Zhang, Z. Ren, Q. Shi, W. Liu, C. Lee, *Nano Energy* **2020**, *73*, 104760; g) Z. Zhao, Y. Dai, D. Liu, L. Zhou, S. Li, Z. L. Wang, J. Wang, *Nat. Commun.* **2020**, *11*, 6186.